





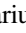



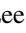
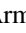




Reconstructing the EUV Spectrum of Star-forming Regions from Millimeter Recombination Lines of H I, He I, and He II

Lena Murchikova¹ , Eric J. Murphy² , Dariusz C. Lis³ , Lee Armus⁴ , Selma de Mink^{5,6} , Kartik Sheth⁷ ,
Nadia Zakamska⁸ , Frank Tramper⁹ , Angela Bongiorno¹⁰ , Martin Elvis⁶ , Lisa Kewley¹¹ , and Hugues Sana¹² 

¹Institute for Advanced Study, 1 Einstein Drive, Princeton, NJ 08540, USA; lena@ias.edu

²National Radio Astronomy Observatory 520 Edgemont Road, Charlottesville, VA 22903, USA

³Jet Propulsion Laboratory, California Institute of Technology, 4800 Oak Grove Drive, Pasadena, CA 91109, USA

⁴Infrared Processing and Analysis Center, MC 314-6, 1200 E. California Boulevard, Pasadena, CA 91125, USA

⁵Anton Pannekoek Institute for Astronomy, University of Amsterdam, Science Park 904, 1098XH, Amsterdam, The Netherlands

⁶Center for Astrophysics, Harvard Smithsonian, 60 Garden Street, Cambridge, MA 02138, USA

⁷NASA Headquarters, 300 E Street SW, Washington, DC 20546, USA

⁸Department of Physics and Astronomy, Johns Hopkins University, 3400 N. Charles Street, Baltimore, MD 21218, USA

⁹Institute for Astronomy, Astrophysics, Space Applications and Remote Sensing, National Observatory of Athens, Metaxa & Vas. Pavlou Street, 15236, Penteli, Athens, Greece

¹⁰INAF-Osservatorio Astronomico di Roma, Via di Frascati 33, I-00040 Monteporzio Catone, Rome, Italy

¹¹RSAA, Australian National University, Cotter Road, Weston Creek, ACT 2611, Australia

¹²Institute of Astrophysics, Universiteit Leuven, Celestijnenlaan 200 D, B-3001 Leuven, Belgium

Received 2020 June 26; revised 2020 August 26; accepted 2020 September 7; published 2020 October 29

Abstract

The extreme ultraviolet (EUV) spectra of distant star-forming regions cannot be probed directly using either ground- or space-based telescopes due to the high cross section for interaction of EUV photons with the interstellar medium. This makes EUV spectra poorly constrained. The millimeter/submillimeter recombination lines of H and He, which can be observed from the ground, can serve as a reliable probe of the EUV. Here we present a study based on ALMA observations of three Galactic ultracompact H II regions and the starburst region Sgr B2(M), in which we reconstruct the key parameters of the EUV spectra using millimeter recombination lines of H I, He I, and He II. We find that in all cases the EUV spectra between 13.6 and 54.4 eV have similar frequency dependence: $L_\nu \propto \nu^{-4.5 \pm 0.4}$. We compare the inferred values of the EUV spectral slopes with the values expected for a purely single stellar evolution model (Starburst99) and the Binary Population and Spectral Synthesis code (BPASS). We find that the observed spectral slope differs from the model predictions. This may imply that the fraction of interacting binaries in H II regions is substantially lower than assumed in BPASS. The technique demonstrated here allows one to deduce the EUV spectra of star-forming regions, providing critical insight into photon production rates at $\lambda \leq 912\text{\AA}$, and can serve as calibration to starburst synthesis models, improving our understanding of star formation in the distant universe and the properties of ionizing flux during reionization.

Unified Astronomy Thesaurus concepts: [Astrophysicists \(105\)](#); [Interstellar medium \(847\)](#); [Star forming regions \(1565\)](#); [Star formation \(1569\)](#); [Radiative recombination \(2057\)](#); [Compact H II region \(286\)](#)

1. Introduction

Wherever ionization is taking place, extreme ultraviolet radiation (EUV) $\sim 10\text{ eV} - 100\text{ eV}$ is being emitted and absorbed by gas and dust. However, EUV radiation is notoriously difficult to observe. Due to their large cross section for interaction with the interstellar medium, EUV photons can typically travel no more than several hundred parsecs (Redfield 2006), making direct observations of EUV spectra of distant star-forming galaxies impossible. Even for nearby sources, the EUV observations are difficult because EUV photons are easily absorbed by the Earth's atmosphere, so they can only be observed from space. Instruments in space are currently quite limited in their wavelength coverage and spectral resolution (Werner 2010), therefore accurate indirect methods of determining the EUV fluxes of astronomical sources are very valuable.

Young stellar populations containing massive stars largely determine the radiative properties of star-forming galaxies and are the primary source of ionizing radiation, in the absence of an active central supermassive black hole, e.g., Baldwin et al. (1981), González Delgado et al. (1999), Shull et al. (2012). Optical emission lines, e.g., through BPT diagrams (Baldwin et al. 1981;

Veilleux & Osterbrock 1987), are often used to indicate the presence of an underlying star-forming population. The total production rates of ionizing EUV photons by young star clusters are often determined from visible wavelength H α and H β emission line fluxes or from radio free-free continuum emission (e.g., Murphy et al. 2012; Linden et al. 2020; Murphy et al. 2017). As a result, quantitative relationships between line fluxes and the underlying EUV fluxes are often made difficult by extinction uncertainties.

Uncertain EUV fluxes are a big concern for widely used spectral synthesis codes such as Starburst99 (Leitherer et al. 1999, 2014). Recently, stellar evolutionary models have been improved by more realistic treatment of mass loss, stellar rotation, binarity, and the upper stellar mass limit (Maeder & Meynet 2000; Vink 2000; de Mink et al. 2009; Crowther et al. 2016). This new generation of models, however, shows large discrepancies in the extreme UV (Levesque et al. 2012; Stanway et al. 2016; Eldridge et al. 2017) due to stellar wind mass loss, model atmosphere uncertainties (see Figure 4 of Leitherer (2012)), and most importantly, whether there are Wolf-Rayet stars present. The latter, being very hot ($\sim 50,000 - 200,000\text{ K}$) and of high luminosity, can increase the

hard EUV luminosity by 2–4 orders of magnitude. The incidence of Wolf–Rayet stars is affected by assumed stellar rotation and binarity and by the adopted upper mass limit.

Empirical methods are needed to reconstruct accurate EUV properties of star formation to bring us closer to understanding star formation in finer detail, and to provide critical input for testing and constraining population-synthesis models. This in turn impacts cosmological and galaxy formation simulations, which rely on synthesis codes for treatment of subgrid physics input: ionizing fluxes and radiative feedback, as well as for interpretations of the observations of galaxies in the local Universe and at high redshift.

Such a probe of EUV spectra can be provided by the millimeter/submillimeter recombination lines of H I, He I, and He II. These lines can probe the EUV spectrum at energies >13.6 eV, >24.6 eV, and >54.4 eV, corresponding to the ionization threshold of H I, He I, and He II, respectively. These lines circumvent all of the problems with other indirect probes: (1) they are at sufficiently long wavelengths that the dust opacity should be negligible; (2) they are permitted transitions with high critical densities (populated by recombination and radiative decay); (3) they do not have significant maser amplification (an issue for cm-wave recombination lines); and (4) they are emitted by H and He and thus do not depend on metallicity (Scoville & Murchikova 2013, hereafter SM13).

The theoretical analysis of SM13 indicates that the millimeter/submillimeter line fluxes provide reliable estimates of the emission measures of H II and He II, which we extend here to He III. Using these emission measures one can then estimate the ionizing continua of H I, He I, and He II, assuming radiative equilibrium. Since these lines are ionized at different photon energies, by comparing the ionizing continua of these three species one can derive the underlying EUV spectrum. We are particularly interested in the so-called α -transitions, $n + 1 \rightarrow n$ transitions of neutral hydrogen H, neutral He, and of single-ionized He (see SM13). Over the density range $n_e = 10^2$ – 10^8 cm $^{-3}$, the emissivities of the α lines of H I, He I, and He II at $n \sim 30$ vary by less than 20%, and variations with T_e are also small.

In this work we report the result of an Atacama Large Millimeter/submillimeter Array (ALMA) observing program demonstrating the potential of millimeter/submillimeter lines of H I, He I, and He II to reveal the underlying EUV spectrum. To this end we use a sample of three ultracompact H II regions and one massive starburst region (i.e., a region containing multiple H II regions). The intrinsic dusty environment of compact star-forming regions makes observations in millimeter/submillimeter lines particularly advantageous.

The paper is organized as follows. In Section 2 we discuss the theory of using the recombination lines of H I, He I, and He II to constrain the EUV spectra. In Section 3 we describe the observations and data reduction. In Section 4 we discuss the data analysis. In Section 5 we discuss the physical implication of the obtained EUV spectra and compare them with simulations. We use BPASS v2.2.1 and Starburst 99 v7.0.1. In Appendix we calculate the production rate of EUV photons and derive the properties of EUV spectra.

2. Theory

In this section we derive the intrinsic EUV spectra inside a star-forming (SF) region using observed millimeter recombination lines fluxes of H30 α , He30 α , and He $^{+}$ 48 α . Any three

millimeter/submillimeter recombination lines of H I, He I, and He II may be used, but these three particular lines are chosen here because they can be observed simultaneously with ALMA, and thus are favorable from the point of view of reducing the telescope time. Below we first convert the observed velocity-integrated line fluxes into a volume emission measure, then assuming radiation equilibrium, derive the production rates of EUV photons, and then derive the EUV spectral parameters.

The velocity-integrated line flux $[S\Delta V]_{\mathcal{L}}$ in millimeter/submillimeter recombination line \mathcal{L} from a SF region is directly proportional to the volume emission measure EM_x of the ion x , which produces the line \mathcal{L} while recombining with e^- through a recombination cascade (SM13):

$$[S\Delta V]_{\mathcal{L}} = \frac{\varepsilon_{\mathcal{L}}}{4\pi D^2} EM_x \frac{c}{\nu_{\mathcal{L}}}. \quad (1)$$

Here $[S\Delta V]_{\mathcal{L}} = \int S_{\mathcal{L}}(V) dV$ is the velocity-integrated line flux, $S_{\mathcal{L}}(V)$ is the flux in the \mathcal{L} line at velocity V , $\varepsilon_{\mathcal{L}}$ is the emissivity of the recombination line \mathcal{L} , D is the distance to the source, c is the speed of light, and $\nu_{\mathcal{L}}$ is the frequency of line \mathcal{L} . The volume emission measure is defined as $EM_x = n_x n_e \text{vol}_x$, n_x is density of ion x , n_e is electron density in the region, and vol_x is volume of space taken by the region where species x is present. In our observations we specifically consider $x = \text{H II}$, He II, He III, and $\mathcal{L} = \{\text{H}30\alpha: n = 31 \rightarrow 30\}, \{\text{He}30\alpha: n = 31 \rightarrow 30\}, \{\text{He}^{+}48\alpha: n = 49 \rightarrow 48\}$.

The line frequencies and emissivities of the observed recombination lines H30 α , He30 α , and He $^{+}$ 48 α at typical densities $n \sim 10^4$ cm $^{-3}$ and temperatures $T \sim 10^4$ K inside H II regions are as follows (Storey & Hummer 1995a, 1995b):

$$\begin{aligned} \text{H}30\alpha: \nu_{\text{H}30\alpha} &= 231.901 \text{ GHz}, \\ \varepsilon_{\text{H}30\alpha} &= 1.05 \times 10^{-31} \text{ erg cm}^3 \text{ s}^{-1} \\ \text{He}30\alpha: \nu_{\text{He}30\alpha} &= 231.995 \text{ GHz}, \\ \varepsilon_{\text{He}30\alpha} &= 1.05 \times 10^{-31} \text{ erg cm}^3 \text{ s}^{-1} \\ \text{He}^{+}48\alpha: \nu_{\text{He}^{+}48\alpha} &= 230.713 \text{ GHz}, \\ \varepsilon_{\text{He}^{+}48\alpha} &= 3.67 \times 10^{-31} \text{ erg cm}^3 \text{ s}^{-1}. \end{aligned} \quad (2)$$

While the values of $\varepsilon_{\text{H}30\alpha}$ and $\varepsilon_{\text{He}^{+}48\alpha}$ are tabulated in the literature, to estimate the value of $\varepsilon_{\text{He}30\alpha}$ we use the fact that at $n \sim 30$, the He I atom can also be considered a hydrogenic ion, as the second electron is close to the nucleus and is screening its charge. Then we can use the scaling relation $\varepsilon_{\text{He}n\alpha}(T, n) \simeq Z_{\text{eff}}^{17/3} \varepsilon_{\text{H}n\alpha}(T, n)$ derived in SM13 Appendix C and assume $Z_{\text{eff}} = 1.0002$ for the effective charge of the nucleus (Towle et al. 1996).

From Equations (1) and (2) we find

$$\begin{bmatrix} \frac{EM_{\text{H II}}}{\text{cm}^{-3}} \\ \frac{EM_{\text{He II}}}{\text{cm}^{-3}} \\ \frac{EM_{\text{He III}}}{\text{cm}^{-3}} \end{bmatrix} = \begin{bmatrix} 8.81 \\ 8.81 \\ 2.51 \end{bmatrix} \times 10^{57} \begin{bmatrix} \frac{[S\Delta V]_{\text{H}30\alpha}}{\text{Jy km s}^{-1}} \\ \frac{[S\Delta V]_{\text{He}30\alpha}}{\text{Jy km s}^{-1}} \\ \frac{[S\Delta V]_{\text{He}^{+}48\alpha}}{\text{Jy km s}^{-1}} \end{bmatrix} \left(\frac{D}{\text{kpc}} \right)^2. \quad (3)$$

To keep the amount of gas constituting the EMs ionized we need an influx of ionizing photons above the ionization threshold (13.6 eV, 24.6 eV and 54.4 eV for H I, He I, and

Table 1
Observed H II Regions

Name	R.A.	Decl.	Distance	Ang. scale	ALMA Cycle
G330.9536	16:09:52.60	-51:54:55	5.5 kpc	~2"	2 & 4
G332.8254	16:20:11.00	-50:53:16	4.4 kpc	~3"	2 & 4
SgrB2(M)	17:47:20.15	-28:23:05	8.3 kpc	~2" × 4"	2
G328.8076	15:55:48.60	-52:43:07	11.7 kpc	~4"	2

Note. This table lists the H II regions selected for this study, their positions, distances, angular scale, and the ALMA Cycle they were observed in.

He II, respectively) sufficient to counteract recombination. Then, following [Appendix](#), we can use the following approximate relations:

$$\begin{bmatrix} \frac{Q_0}{\text{s}^{-1}} \\ \frac{Q_1}{\text{s}^{-1}} \\ \frac{Q_2}{\text{s}^{-1}} \end{bmatrix} \simeq \begin{bmatrix} 2.59 \\ 2.72 \\ 18.5 \end{bmatrix} \times 10^{-13} \begin{bmatrix} \frac{\text{EM}_{\text{H II}}}{\text{cm}^{-3}} \\ \frac{\text{EM}_{\text{He II}}}{\text{cm}^{-3}} \\ \frac{\text{EM}_{\text{He III}}}{\text{cm}^{-3}} \end{bmatrix}. \quad (4)$$

Here we use the standard notations for the photon production rates above the H I, He I, and He II ionization thresholds:

$$\begin{aligned} Q_0 &= \int_{\nu_0}^{\infty} \frac{L_\nu}{h\nu} d\nu, & Q_1 &= \int_{\nu_1}^{\infty} \frac{L_\nu}{h\nu} d\nu, \\ Q_2 &= \int_{\nu_2}^{\infty} \frac{L_\nu}{h\nu} d\nu, \end{aligned} \quad (5)$$

where L_ν is the specific luminosity of all the stars within the region and $h\nu_0 = 13.6$ eV, $h\nu_1 = 24.6$ eV, and $h\nu_2 = 54.4$ eV.

Now we need to assume a model for the EUV spectrum inside SF regions. Due to the effects of stellar atmospheres it is natural to approximate the EUV spectrum for photons with energies higher than 13.6 eV as a three-component power law. The first break at 24.6 eV corresponds to the ionization threshold of He I and the second break at 54.4 eV corresponds to the ionization threshold of He II. Such a model, however, has four free parameters—the absolute value of the spectra at 13.6 eV, the spectral slope between 13.6 eV and 24.6 eV, the spectral slope between 24.6 eV and 54.4 eV, and the spectral slope above 54.4 eV. Our observations provide us with three observed parameters (see Equations (3)), and thus an ability to determine three model parameters. Consequently, we need to eliminate one of the free model parameters. We further assume that the EUV spectrum inside SF regions is well-described by a characteristic broken power law with two distinct spectral slopes, the first of which is γ , the EUV spectral slope between energies 13.6 eV and 54.4 eV, and the second is γ_2 —the slope for energies higher than 54.4 eV. Thus we find (see [Appendix](#))

$$L_\nu = \begin{cases} 1.716 \times 10^{22} \text{ erg s}^{-1} \text{ Hz}^{-1} \left(\frac{\text{EM}_{\text{H III}}}{10^{61} \text{ cm}^{-3}} \right) \frac{\gamma}{1 - 0.25^\gamma} \left(\frac{\nu}{\nu_0} \right)^{-\gamma}, & \nu_0 \leq \nu < \nu_2 \\ L_2 (\nu/\nu_2)^{-\gamma_2}, & \nu \geq \nu_2, \end{cases} \quad (6)$$

where

$$\gamma_2 \simeq 1.4 \times 10^2 \left(\frac{\text{EM}_{\text{H II}}}{10^{61} \text{ cm}^{-3}} \right) \left(\frac{\text{EM}_{\text{He III}}}{10^{58} \text{ cm}^{-3}} \right)^{-1} \frac{\gamma}{4^\gamma - 1} \quad (7)$$

γ is the solution of the equation

$$\frac{2.21^\gamma - 1}{4^\gamma - 1} \simeq 0.105 \left(\frac{\text{EM}_{\text{He II}}}{10^{60} \text{ cm}^{-3}} \right) \left(\frac{\text{EM}_{\text{H II}}}{10^{61} \text{ cm}^{-3}} \right)^{-1}. \quad (8)$$

and from the continuity requirement we get

$$L_2 = 1.716 \times 10^{22} \frac{\text{erg}}{\text{s Hz}} \left(\frac{\text{EM}_{\text{H III}}}{10^{61} \text{ cm}^{-3}} \right) \frac{\gamma}{4^\gamma - 1}. \quad (9)$$

3. Observations and Data Reduction

We present results from ALMA observations. Our data were obtained during two ALMA observational programs: Cycle 2 project 2013.1.00111.S and Cycle 4 project 2016.1.01015.S. [Table 1](#) lists the names of the observed H II regions, their coordinates, the distances to the sources, and the ALMA Cycle number in which the data were taken.

For the initial set of observations in ALMA Cycle 2, the target list included four OB star formation regions in our Galaxy: three ultracompact H II regions G330.9536, G332.8254, and G328.8076 and the very massive starburst Sgr B2(M), which consists of several H II regions. The three ultracompact H II regions were taken from the survey of [Murphy et al. \(2010\)](#). They were selected for their high luminosity and compactness as well as their location in the southern hemisphere to be most convenient for ALMA observations. Compactness is desired observationally so there would be no concerns about needing extra baselines, and thus observations in additional configurations, to recover extended faint structure, and physically so that the ionized regions are likely to be ionization-bounded with most of the EUV continuum absorbed.

We chose specific recombination lines in this study to avoid confusion with known possible molecular lines by generating model molecular line spectral scans for the Ori-IRc2 ([Crockett et al. 2014](#)) obtained specifically for this project. Among the possible lines, H30 α , He30 α , and He⁺48 α lines can be observed simultaneously with ALMA Band 6, making them our preferred choice. Other possible lines include H26 α with the corresponding He26 α and He⁺49 α .

The three recombination lines H30 α (H I: $n = 31 \rightarrow 30$ at 231.901 GHz), He30 α (He I: $n = 31 \rightarrow 30$ at 231.995 GHz),

and He⁺48 α (He II: $n = 49 \rightarrow 48$ at 230.713 GHz) were observed simultaneously in one tuning of ALMA in Band 6 with two spectrometers with a velocity resolution of 2.5 km s⁻¹. The first spectrometer was set to observe the H30 α and the He30 α

recombination lines and the second was set to the $\text{He}^+48\alpha$ line. The other three spectral windows were set to observe the continuum at 232.8 GHz, 232.3 GHz, and 229.9 GHz with a velocity resolution of 40 km s^{-1} . The continuum is expected to be a mixture of free–free emission and thermal dust emission. The spectral setup was the same in all of our observations.

The observations in ALMA Cycle 2 were conducted on 2015 April 23 (Sgr B2 (M)) with 38 antennas and achieved a resolution of $1''.24 \times 0''.93$; on 2015 April 24 and 27 (G328.8076, G330.9536, and G332.8254) with 38 antennas and achieved a resolution of $0''.53 \times 0''.47$, and on 2015 June 16 (Sgr B2(M)) with 30 antennas and achieved a resolution $0''.53 \times 0''.47$. The exposure times on target were 9 min on each of the G-sources and 18 min total on Sgr B2(M). The achieved sensitivity is 2 mJy/beam in a 10 km s^{-1} velocity channel in each source. We used the calibration and data reduction scripts prepared by the staff at North American ALMA Science Center (NAASC) in Charlottesville, Virginia. We imaged and CLEANed the data using the Common Astronomy Software Applications package (CASA). The images created were 500×500 pixel with the pixel size $0''.08$. In all observed sources the HI recombination line was clearly detected.

For the deeper observations in ALMA Cycle 4 we selected the two most $\text{H}30\alpha$ -luminous and the sources least contaminated by molecular lines—G330.9536 and G332.8254. The observations of G330.9536 and G332.8254 in ALMA Cycle 4 were conducted on May 6 and 8, 2017 with 47 antennas and May 7, 2017 with 50 antennas. The achieved resolution was $\sim 0''.3 \times 0''.28$. The total exposure time on each target was ~ 120 min. The achieved sensitivity is 0.4 mJy/beam in a 10 km s^{-1} velocity channel in each source. For calibration and data reduction we used the script automatically generated by the ALMA pipeline provided by the NAASC. We imaged the data using the task `tclean` in CASA. The images created were 1000×1000 pixel with the pixel size $0''.028$. In all the observed sources the HI and He I recombination lines was clearly detected. We set a limit on He II recombination-line emission. The maximum recoverable scale of the emission is $\sim 3''.5$.

4. Data Analysis

After imaging the data as described above we identified the line-free channels. The H II regions in general have an abundance of molecular and atomic features. Therefore, it is important to identify the channels for continuum subtraction carefully, rather than identifying wide frequency ranges outside the recombination lines of interest. Then we performed subtraction of the continuum in the uv -plane with the `uvcontsub` task in CASA using the identified channels to obtain separate continuum and line images (Figure 1).

We selected several of the $\text{H}30\alpha$ -brightest subregions, as well as identified large regions called “ $\text{tot}_{\text{H}30\alpha}$ ” encapsulating most of the $\text{H}30\alpha$ emission. Extraction regions are shown in Figure 3. While the extraction region “ $\text{tot}_{\text{H}30\alpha}$ ” encapsulates most of the $\text{H}30\alpha$ emission, it does not necessarily contain most of the continuum emission. Some of the targets contain multiple nonoverlapping subregions, each of which can be considered as an independent probe of the underlying EUV spectrum. We extract spectra within these subregions and analyze them. An example spectrum for each target is shown in Figure 2.

Computation of the velocity-integrated line flux can be achieved by integrating under the recombination line. However, in order to obtain accurate values we need to remove contributions of molecular lines. Molecular lines are easily identifiable in most cases by their much narrower width. To remove contributions of molecular lines to velocity-integrated line flux of the recombination lines, we fitted the spectra with a combination of Gaussian and Voigt profiles and then used the fit to extract the central velocity (V) of the $\text{H}30\alpha$ and $\text{He}30\alpha$ lines, their width (ΔV), and the velocity-integrated line flux ($[S\Delta V]_{\mathcal{L}}$). In the cases when the He I line is positioned on the wing of the HI line, we fit the HI line first, then subtract its contribution from the He I line and fit the He I line with the Gaussian or a combination of Gaussian and Voigt profiles in the same way as the HI line.

The He II recombination line was not detected in any of our targets. This is expected, as the number of $h\nu > 54.4 \text{ eV}$ photons is predicted to be quite low in SF regions (see below). To set the limit on $[S\Delta V]_{\text{He}^+48\alpha}$ we assume that $V_{\text{He}^+48\alpha} = V_{\text{H}30\alpha} \simeq V_{\text{He}30\alpha}$ and $\Delta V_{\text{He}^+48\alpha} = \Delta V_{\text{He}30\alpha}$. These imply that H II, He II, and He III Stromgren spheres are at rest with respect to each other and that the bulk motions of the gas, which dominate the line recombination width (see below) within He II and He III Stromgren spheres, are similar. The derivation of the $\text{He}^+48\alpha$ flux limit is also complicated by the presence of strong molecular features on both sides of the line at about $\pm 50 \text{ km s}^{-1}$. Thus, instead of integrating the expected velocity range around the central frequency we use the width and the velocity of $\text{He}30\alpha$ lines to obtain the expected $\text{He}^+48\alpha$ profile, which we then fit under the uncontaminated spectral data points around the central frequency.

The results of the measurements and calculations are given in Table 2. The line-of-sight thermal velocities of H and He atoms at the characteristic temperature of H II regions of $T \sim 10^4 \text{ K}$ are $\bar{V}_z^{\text{H}} \sim 9 \text{ km s}^{-1}$ and $\bar{V}_z^{\text{He}} \sim 4.5 \text{ km s}^{-1}$, a factor of a few less than the observed line widths. This is due to the fact that a considerable part of the motion reflected in the recombination lines’ widths is due to the bulk motion of the gas (inflow, outflow, rotation), blending of components, etc.

We present continuum flux densities within the extraction regions (S_{cont}) in Table 2. The continuum flux densities can be used in conjunction with the recombination-line fluxes to estimate the temperature within the H II regions. To do this one assumes that most continuum radiation is coming from the free–free emission. The temperature estimates for the observed extraction regions obtained this way are between 5,000 K to 12,000 K, in agreement with the temperatures expected within H II regions. A caveat in these estimates, however, is that the continuum emission in such dusty sources as our H II regions is a combination of free–free emission and dust emission and they cannot be separated without extensive multiwavelength coverage. Thus the temperatures estimated as discussed above are highly uncertain, and we opt to omit discussing them in detail.

We estimate the uncertainties of the line width and the central line velocity at $\delta V = 2.5 \text{ km s}^{-1}$. The uncertainties on the velocity-integrated line flux are $\delta[S\Delta V] \sim 0.01 \text{ Jy km s}^{-1}$ in the Cycle 4 observations and $\delta[S\Delta V] \sim 0.1 \text{ Jy km s}^{-1}$ in the Cycle 2 observations. The accuracy of determining $[S\Delta V]$, V , and ΔV is dominated by molecular lines, contamination, which is hard to quantify.

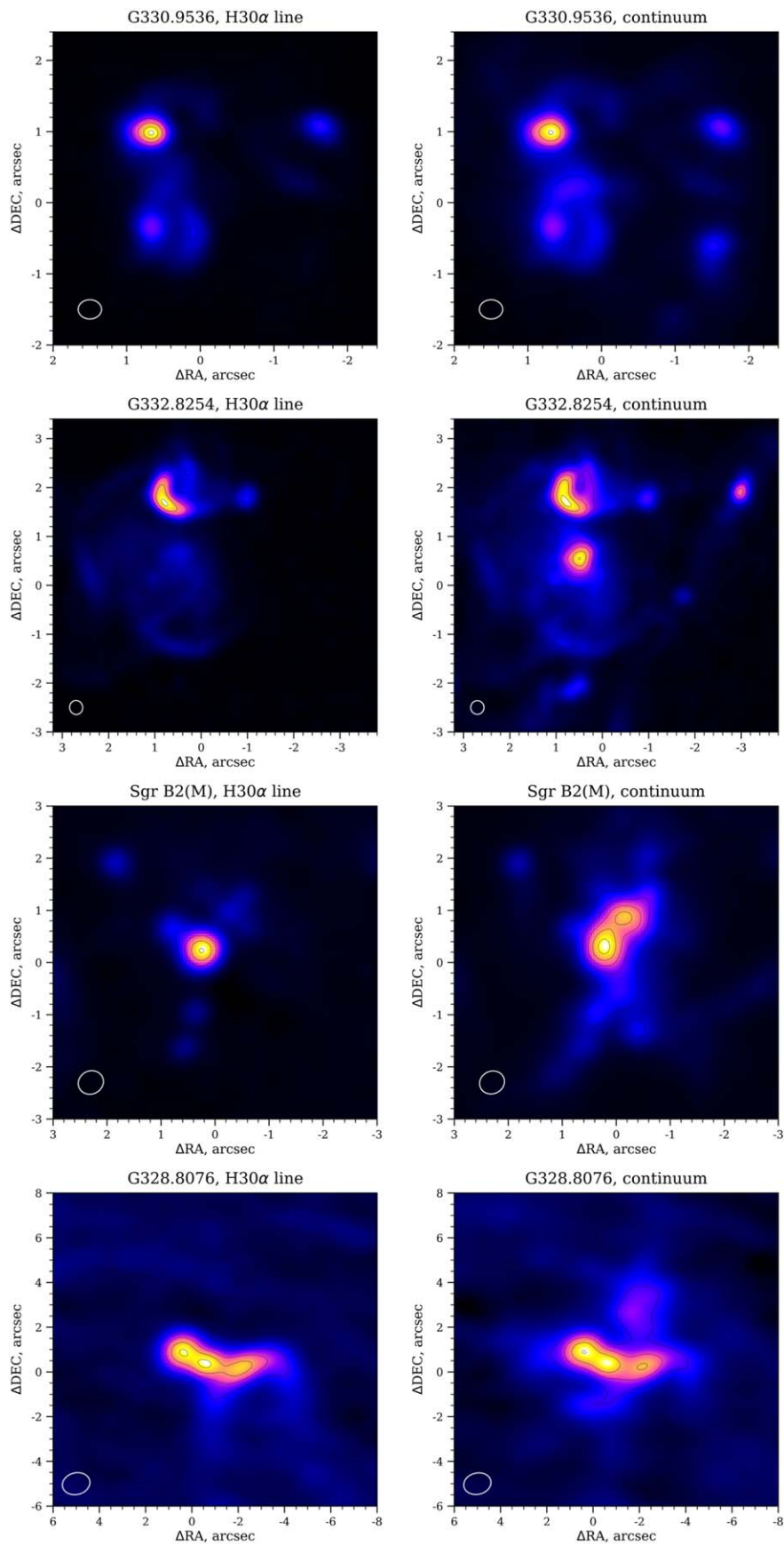


Figure 1. Continuum-subtracted H 30α line flux maps (left) and continuum maps (right) of the Galactic H II regions G330.9536, G332.8254, and G328.8076, and the massive starburst Sgr B2 (M). The beams sizes are plotted in the bottom left corner of each panel.

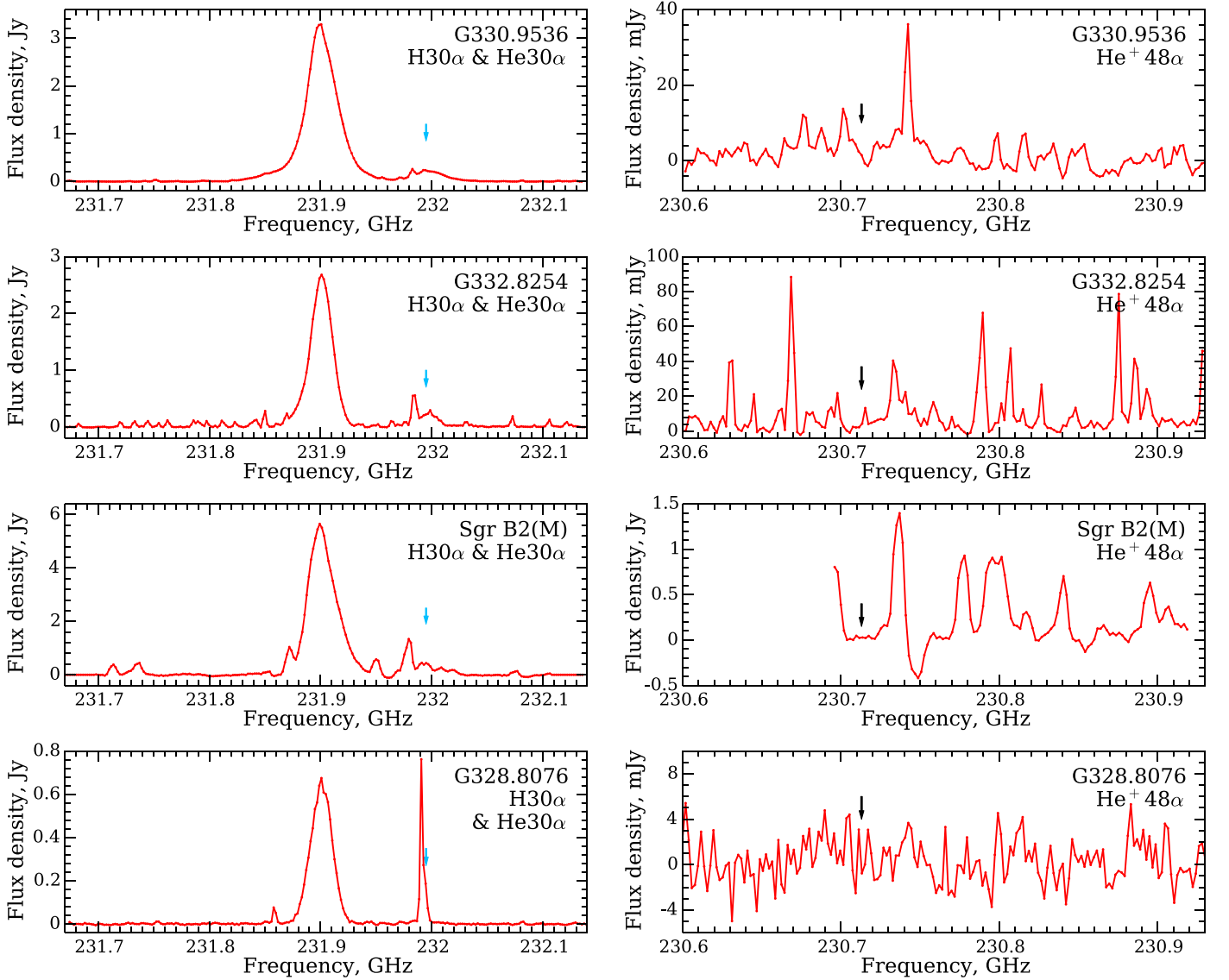


Figure 2. Spectra of the brightest subregions of the H II regions G330.9536, G332.8254, Sgr B2(M), and G328.8076. The spectra are given in the rest frame of their respective sources. Left panels: the strong wide peaks at 231.9 GHz are H30 α lines. The weak wide peaks at 231.995 GHz marked with blue arrows are He30 α lines. The rest of the features in the spectra are molecular lines, which are much narrower than H30 α and He30 α . The strong and narrow feature just to the left from G328.8076’s He30 α line is a molecular line. Right panels: black arrows mark the central frequency of the undetected He⁺48 α line. The level of spectral noise is ~ 0.5 mJy per 10 km s⁻¹ channel for G330.9536 and G332.8254, and 2 mJy per 10 km s⁻¹ channel for Sgr B2(M) and G328.8076, so most of the features, for example, in G332.8254 are molecular lines, not noise. All spectra here are given for extraction 1 of their respective sources (see Figure 3).

For G330.9536 and G332.8254 we estimate the combined uncertainty on $[S\Delta V]_{\text{H}30\alpha}$ at 3%, the uncertainty on $[S\Delta V]_{\text{He}30\alpha}$ at 10% and the uncertainty on $[S\Delta V]_{\text{He}^+48\alpha}$ at 30%. For G328.8076 and Sgr B2(M) we estimate the combined uncertainty on $[S\Delta V]_{\text{H}30\alpha}$ at 5%, the uncertainty on the limit on $[S\Delta V]_{\text{He}30\alpha}$ at 30%, and the uncertainty on $[S\Delta V]_{\text{He}^+48\alpha}$ at 50%. We calculate each velocity-integrated line flux using the procedure described earlier in this section. In the spectrum of G328.8076 we remove all points belonging to the strong and narrow molecular feature just to the left from the He30 α line and fit the Gaussian-like profile to the remaining points. The presence of a strong molecular feature on top of the He30 α line in G328.8076 and the fact that the estimated $[S\Delta V]_{\text{He}30\alpha}$ for all subregions are comparable with the observational uncertainties make the derived values of γ for this target unreliable.

The uncertainties in $[S\Delta V]_{\mathcal{L}}$ directly translate into uncertainties on $\text{EM}_{\mathcal{L}}$ via Equation (3), into Q ’s via Equation (4), and

to L_{ν} , γ and γ_2 via Equation (6), implying uncertainty of $\sim 4\%$ on γ for the Cycle 4 targets and of $\sim 10\%$ on Sgr B2(M). Since the equations are approximate, we expect the true uncertainties on the derived spectral parameters to be $\sim 20\%$. We are unable to provide a meaningful limit on γ_2 for G328.8076 and Sgr B2(M).

5. Discussion

In Table 2 we present derived values for the volume emission measures of H II, He II, and He III (Equation (3)), the production rate of EUV photons Q_0 : $h\nu > h\nu_0 = 13.6$ eV, Q_1 : $h\nu > h\nu_1 = 24.6$ eV, Q_2 : $h\nu > h\nu_2 = 54.4$ eV (Equation (4)) and the inferred parameters of the underlying EUV spectra L_{ν} , γ , and γ_2 (Equation (6)) for each extraction region of G330.9536, G332.8254, Sgr B2(M), and G328.8076 (Figures 1 and 3). We see that for all extraction regions the specific luminosity of EUV for 13.6 eV $\leq h\nu < 54.4$ eV scales close to $L_{\nu} \sim \nu^{-4.5 \pm 0.4}$, and

Table 2
Parameters of the Observed Star-forming Regions

Reg. name	S_{cont} Jy	$V_{\text{H I}}$ km s ⁻¹	$\Delta V_{\text{H I}}$ km s ⁻¹	$[S\Delta V]_{\text{H}30\alpha}$ Jy km s ⁻¹	$\frac{\text{EM}_{\text{H II}}}{10^{61}}$ cm ⁻³	$\frac{Q_0}{10^{48}}$ s ⁻¹	$V_{\text{He I}}$ km s ⁻¹	$\Delta V_{\text{He I}}$ km s ⁻¹	$[S\Delta V]_{\text{He}30\alpha}$ Jy km s ⁻¹	$\frac{\text{EM}_{\text{He II}}}{10^{60}}$ cm ⁻³	$\frac{Q_1}{10^{47}}$ s ⁻¹	$[S\Delta V]_{\text{He}^+48\alpha}$ Jy km s ⁻¹	$\frac{\text{EM}_{\text{He III}}}{10^{58}}$ cm ⁻³	$\frac{Q_2}{10^{46}}$ s ⁻¹	$\frac{L_0}{10^{23}}$ $\frac{\text{erg}}{\text{s Hz}}$	γ	γ_2
G330.9536																	
1	1.43	-90.0	42.5	146.70	3.91	10.12	-92.3	41.5	8.75	2.33	6.34	<0.04	<0.34	<0.62	1.86	4.6	>12
1a	1.81	-90.8	42.8	170.72	4.55	11.78	-91.9	45.4	11.59	3.09	8.40	<0.10	<0.73	<1.36	2.34	4.4	>9
2	0.77	-92.8	30.6	62.72	1.67	4.33	-93.3	32.9	5.50	1.47	4.00	<0.03	<0.19	<0.34	1.00	3.9	>21
3	0.54	-83.1	42.9	41.57	1.11	2.87	-83.9	37.8	2.31	0.62	1.69	<0.07	<0.05	<0.10	0.51	4.7	>20
tot _{H30α}	7.01	-89.7	35.2	485.04	12.93	33.49	-88.2	39.9	34.36	9.17	24.94	<0.13	<0.97	<1.79	6.83	4.3	>20
G332.8254																	
1	1.02	-64.7	30.1	85.46	1.46	3.78	-66.7	26.7	6.48	1.11	3.02	<0.08	<0.39	<0.72	0.80	4.2	>6.5
1a	1.98	-63.7	33.4	147.63	2.52	6.53	-66.6	28.5	10.25	1.75	4.76	<0.21	<1.01	<1.87	1.31	4.4	>3.4
tot _{H30α}	4.75	-64.0	31.0	275.78	4.71	12.20	-68.4	21.8	21.26	3.63	9.87	<1.58	<2.82	<5.21	2.61	4.2	>3.0
Sgr B2(M)																	
1	3.92	51.8	38.5	217.48	13.21	34.21	52	39	12.29	7.47	20.32	<1.434	<24.79	<45	6.07	4.7	...
2	0.43	55.2	40.9	32.42	1.97	5.10	55	41	1.83	1.11	3.02	<0.435	<7.52	<14	0.90	4.7	...
tot _{H30α}	5.49	51.7	39.8	268.10	16.28	42.17	52	40	12.71	7.72	21.00	<2.33	<40.26	<75	6.67	5.0	...
G328.8076																	
1	0.25	-51.4	29.2	20.12	2.43	6.29	-50	30	0.35	0.42	1.15	<0.07	<2.41	<4.4	0.49	6.7	...
2	0.21	-57.2	36.2	18.33	2.21	5.72	-57	36	0.15	0.19	0.51	<0.08	<2.65	<4.9	0.25	8.0	...
tot _{H30α}	0.94	-54.1	32.3	72.95	8.80	22.79	-54	32	0.69	0.83	2.26	<0.34	<11.81	<21.8	1.11	7.8	...

Note. Full set of observed parameters of the H30 α , He30 α and He⁺48 α recombination lines. Their central velocities (V), velocity widths (ΔV), velocity-integrated line fluxes ($[S\Delta V]$), derived volume emission measures (EM) (Equation (3)), production rates of ionizing photons (Q) (Equation (4)) and model parameters of the underlying EUV spectra (L_0 , γ , γ_2) (Equation (6)) for compact H II regions G330.9536, G332.8254, and G328.8076, and starburst Sgr B2(M). Extraction regions are shown in Figure 3. Reg. name is the name of the extraction region, i.e., subregion of the studies H II region. S_{cont} is continuum flux measured within the extraction region. For a discussion of the uncertainties, see Section 4.

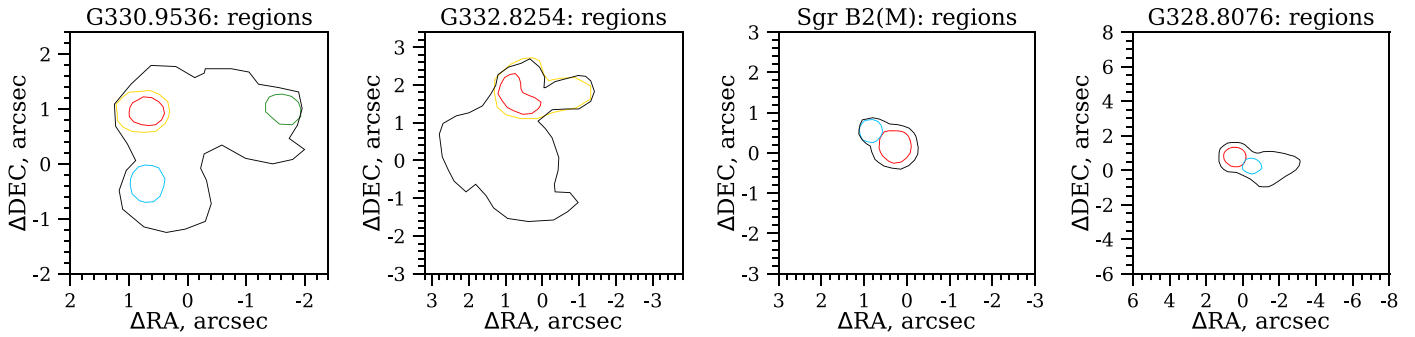


Figure 3. Subregions of the four observed H II regions for which we extract spectra and calculate the intrinsic EUV spectral parameters. Subregion 1 in all targets is marked in red. Yellow marks subregion 1a, which encloses subregion 1. Subregions 2 and 3 are marked in blue and green, respectively. The subregion “totH30 α ” enclosing most of the H30 α emission is marked in black.

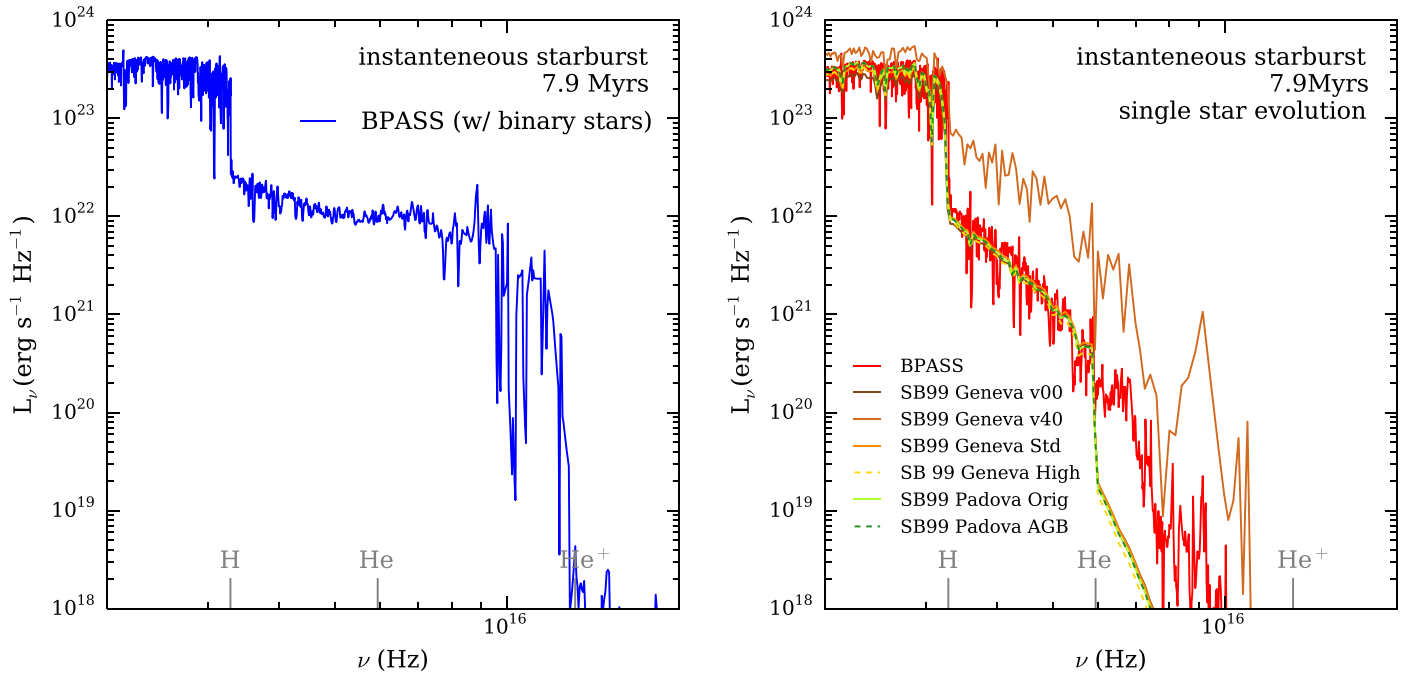


Figure 4. Example spectra of an instantaneous starburst of $10^3 M_{\odot}$ at 7.9 Myr in the models with only single-star evolution—BPASS v2.2.1 single star and various models used in Starburst99 v7.0.1 (right panel) and with binary populations—BPASS v2.2.1 (left panel). In all cases the metallicity is set to $Z = 0.02$, except for Starburst 99 models Geneva v00 and v40, for which only $Z = 0.014$ was available.

steepens even more for higher energies $h\nu \geq 54.4$ eV to $\sim \nu^{-\gamma_2}$, where $\gamma_2 > 15$. The value of the high-energy spectral slope is dominated by G330.9536, which has lower molecular line content and thus allows for much more stringent limit on $[S\Delta V]_{\text{He}^+48\alpha}$ and thus on γ_2 .

Above we quote averaged values of the exponents over the nonoverlapping extraction regions of the observed H II regions excluding G328.8076. The spectral slope γ obtained for G328.8076 is ~ 7.5 . However, the presence of strong molecular line features near He30 α in its spectrum leads to large uncertainties and makes this estimate the least reliable. So we exclude this H II region from the calculation of $\langle \gamma \rangle$ and the following discussion. The 1σ uncertainties of the averaged spectral slope $\langle \gamma \rangle$ quoted above are dominated by the uncertainties of the model assumptions and not the standard deviation due to the averaging.

We compare this observational result with model spectra of an instantaneous $10^3 M_{\odot}$ starburst obtained with (i) Starburst99 v7.0.1 (Leitherer et al. 1999, 2014), which assumes that all stars evolve as single stars only and (ii) the Binary Population

and Spectral Synthesis code (BPASS) v2.2.1 (Eldridge et al. 2017; Stanway & Eldridge 2018), which can take into account binary population and the interactions between the stars such as common envelope evolution and mass transfer. The BPASS can be set to evolve all stars as single stars, i.e., with binary interaction switched off. For illustration we present spectra produced by the two codes at 7.9 Myr in Figure 4. The left panel shows the spectra produced by BPASS with binary interaction included. The right panel shows the spectra for single-star evolution models produced by BPASS with binary interaction switched off and Starburst99 with the six evolutionary tracks—Geneva track with zero rotation (v00), Geneva tracks with $V = 0.4$ rotation (v40), Geneva tracks with standard mass loss, Geneva tracks with high mass loss, original Padova tracks, and Padova tracks with AGB stars. For descriptions and the appropriate references see Leitherer et al. (2014). In all cases the metallicity is set to $Z = 0.02$, except for Starburst 99’s Geneva v00 and v40 tracks, for which only $Z = 0.014$ is available. We scale the simulations to $10^3 M_{\odot}$ so that the production rate of $h\nu > 13.6$ eV photons (Q_0)

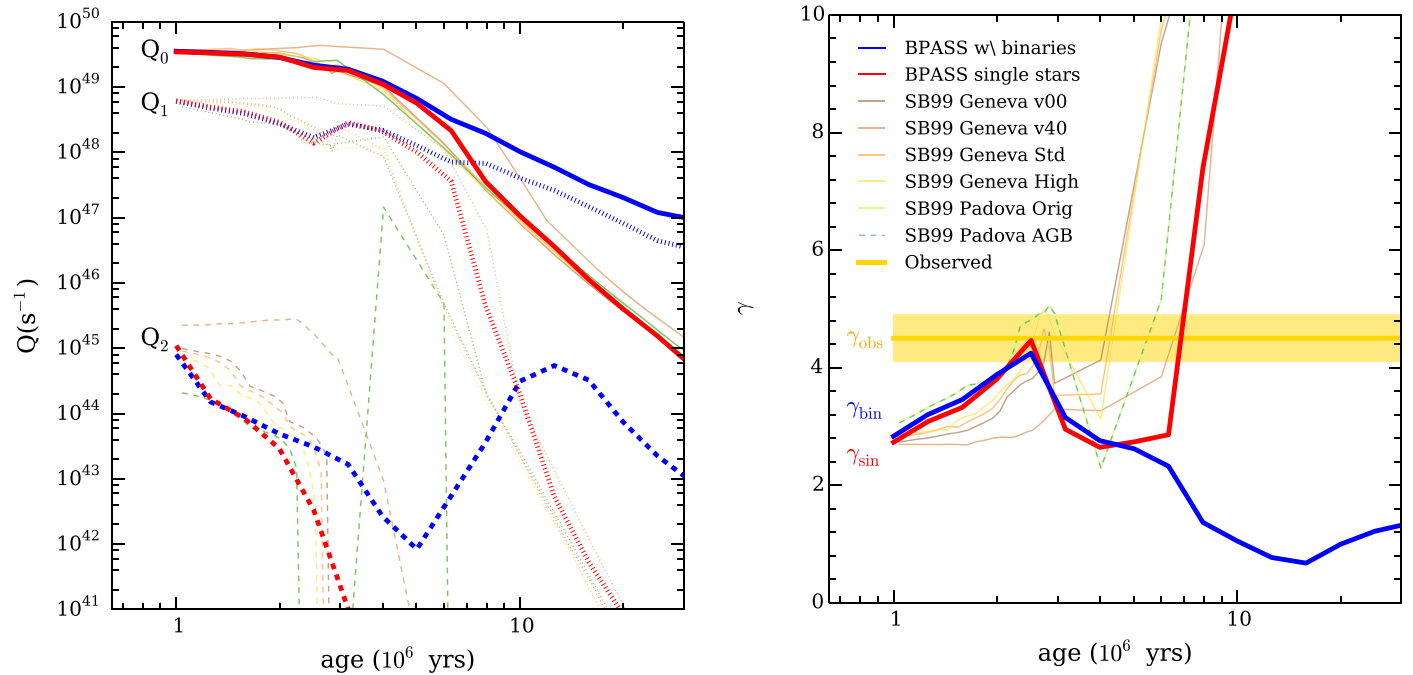


Figure 5. Left panel: the evolution of the production rates of EUV photons with energies above the ionization thresholds of H I, He I, and He II, i.e., $h\nu > 13.6$ eV (Q_0), $h\nu > 24.6$ eV (Q_1) and $h\nu > 54.4$ eV (Q_2), respectively, for instantaneous starbursts scaled to $10^3 M_\odot$ in the models with only single-star evolution—BPASS v2.2.1 single stars (red) and various Starburst99 v7.0.1 models and with binary populations—BPASS v2.2.1 (blue). Right panel: evolution of the slope (γ) of the EUV spectra of $L_\nu \sim \nu^{-\gamma}$, where $13.6 \text{ eV} \leq h\nu < 54.4 \text{ eV}$ for the same models. The values are obtained with Equation (A3). The yellow line marks the average observed value of $\gamma = 4.5 \pm 0.4$.

predicted by the models is similar to the observed values for our extraction regions (see the left panel in Figure 5 and Table 2). The time range on the figure is set to span the lifetime of a single OB star, which is < 30 Myr.

Figure 5 (right panel) shows the evolution of the slope (γ) of the EUV spectra $L_\nu \sim \nu^{-\gamma}$, where $13.6 \text{ eV} \leq h\nu < 54.4 \text{ eV}$, for Starburst99 v7.0.1 (SB99) and BPASS v2.2.1 models. We find that the observed spectral slope $\gamma \simeq 4.5 \pm 0.4$ differs from model predictions. There are no precise enough methods of estimating the absolute age of each SF region, thus we compare the differences between the measured EUV spectral slope and the model for all ages younger than a typical lifetime of an OB star. For an instantaneous starburst of $< 7 \times 10^6$ Myr in age the observationally inferred slopes $\langle \gamma \rangle \simeq 4.5$ are consistently steeper than those in either of the models $\gamma_{\text{sin}} \simeq \gamma_{\text{bin}} \simeq 3$ by a factor of ~ 1.5 , meaning that the observed spectrum is considerably softer than the theoretical one. The values 3 and 4.5 may seem close enough and one may be tempted to declare an agreement between the observations and the simulations. However, it is crucial to stress that we are comparing the values of exponents; and the spectra scaling as ν^{-3} or $\nu^{-4.5}$ are substantially (4 sigma) different from each other. Thus, we conclude that the observations do not agree with the models. For an instantaneous starburst of $> 7 \times 10^6$ Myr the observed spectral slope is in between the two model ones—steeper than γ_{bin} and less steep than γ_{sin} .

Here and below when referring to single-star evolution models we are primarily quoting values produced by a BPASS single star. The Starburst 99 and BPASS single-star evolution models predict similar results for Q_0 , Q_1 and γ . The predictions for Q_2 vary substantially; however, we cannot set any meaningful constraint on these values, as they are below our sensitivity limit. Thus, we do not discuss variations in Q_2 here.

Our observationally inferred EUV spectral slopes for H II regions coincide with the model ones for a ~ 2.5 Myr-old starburst. One may wonder whether this implies that all our H II regions are about the same age, which is ~ 2.5 Myr. We rule out this possibility. The survey by Murphy et al. (2010) identified G330.9536 as an ultracompact or hypercompact H II region, thus its OB stars/clusters of stars are likely at the earliest stage of the evolution. G332.8254 and G328.8076, which are excluded from the discussion, are classified as ultracompact H II, implying that they are larger and thus likely older than G330.9536. Sgr B2(M) consists of several classical well-developed H II regions, placing it at a later evolutionary stage than any of the G-sources. Our H II regions span several stages of H II region evolution and of their embedded OB star population evolution and cannot be of the same age. This makes our finding that all of the EUV spectra have similar shapes as $L_\nu \sim \nu^{-4.5}$ even more puzzling.

Let us now assume that the ages of all our SF regions are > 7 Myr. For simplicity we also assume that the primary difference between the single-star evolution and binary evolution codes is the interacting binary fraction, which is zero for Starburst99 and the BPASS single star and $\sim 60\%$ for massive $\sim 5 M_\odot$ stars, exceeding $\sim 90\%$ for $M > 16 M_\odot$ stars in BPASS v2.2.1 (see Figure 1 of Stanway & Eldridge 2018). The latter is comparable with the 70% estimated by Sana et al. (2012) for O stars. For such ages the observationally determined EUV spectral slope is always in between the two models, i.e., steeper than that for BPASS’s binary evolution model and less steep than that for the Starburst99 and BPASS single-star models. This can imply that the binary fraction also has to be in between the binary fractions assumed in BPASS binary evolution and in Starburst99 or BPASS single star, i.e., lower than in BPASS binary evolution and greater than in Starburst99 or BPASS single star. Let us take as an example a

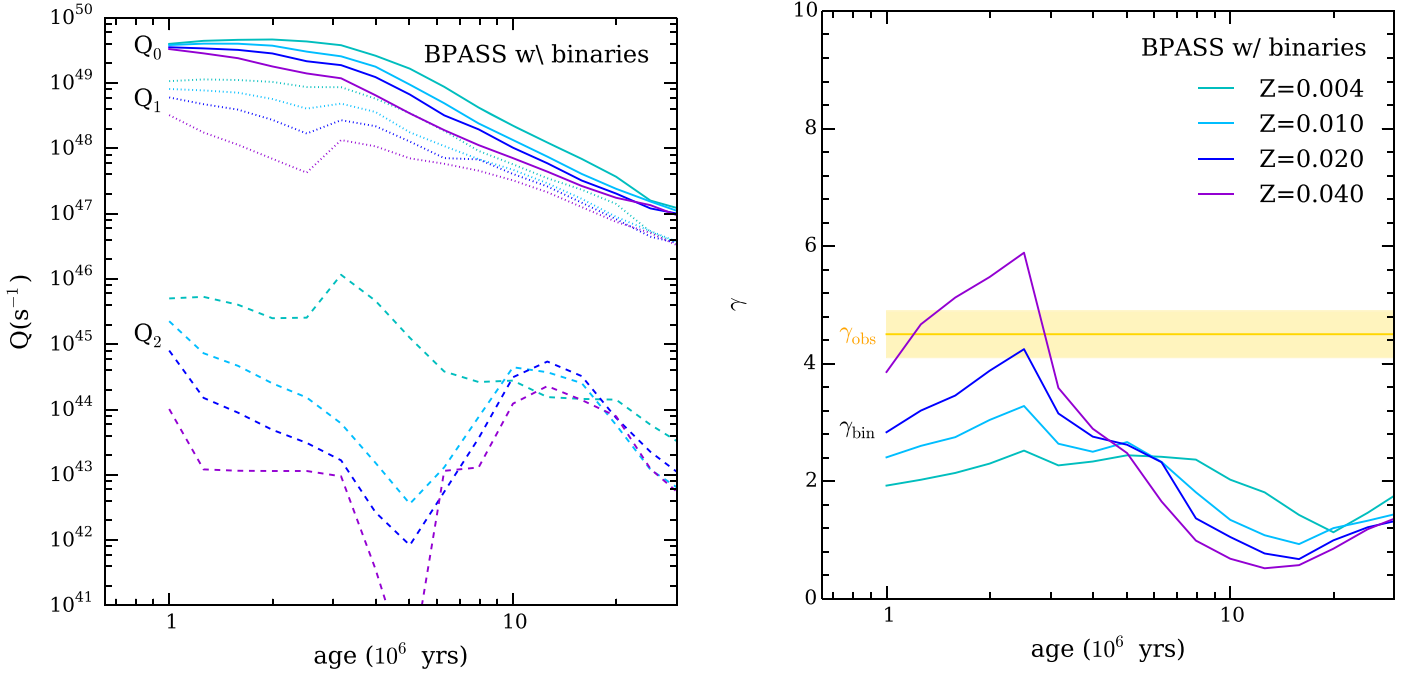


Figure 6. Left panel: the evolution of the production rates of EUV photons with energies above the ionization thresholds of H I, He I, and He II, i.e., $h\nu > 13.6$ eV (Q_0), $h\nu > 24.6$ eV (Q_1), and $h\nu > 54.4$ eV (Q_2), respectively, as a function of metallicity for instantaneous starbursts scaled to $10^3 M_\odot$ in the model with binary populations produced by BPASS v2.2.1. Right panel: evolution of the slope (γ) of the EUV spectra of $L_\nu \sim \nu^{-\gamma}$, where 13.6 eV $\leq h\nu < 54.4$ eV as a function of metallicity for the same models with binary populations produced by BPASS v2.2.1. The values are obtained with Equation (A3). The yellow line marks the average observed value of $\gamma = 4.5 \pm 0.4$.

7.9 Myr-old SF region whose model spectra are presented in Figure 4. At this age the model EUV spectral slope we can infer either from Figure 4 or from Figure 5 (right panel) is $\gamma_{\text{bin}} \simeq 1.5$ and $\gamma_{\text{sin}} \simeq 7.5$ compared to the observed $\gamma = 4.5$, implying that we need to assume a lower binary fraction than assumed in BPASS v2.2.1 (see Figure 1 of Stanway & Eldridge 2018).

EUV spectral slopes in extraction regions of Sgr B2(M) are consistently steeper than those for the G-sources, which may be an indication of spectra steepening with age, similar to the trend predicted by single-star evolution models with its zero binary fraction, while BPASS with binary evolution predicts the spectral slope marginally decreasing at the later stages of evolution while mostly staying at $\gamma_{\text{BPASS}} \sim 1$. This again may serve as an indicator that the binary fraction in the SF regions is likely smaller than 60% for massive $\sim 5 M_\odot$ stars and exceeding $\sim 90\%$ for $M > 16 M_\odot$ stars in BPASS v2.2.1 (Figure 1 of Stanway & Eldridge 2018). Another possibility is that the steepening may be due to partial escape of EUV photons from the region. Our calculations are based on the assumption that all EUV photons are captured and reprocessed into lower-energy recombination-line photons by H and He. This is a particularly good approximation for ultracompact and hypercompact H II regions, but may lead to less accurate estimations for evolved H II regions such as Sgr B2(M), from which photons can escape more easily.

In the analysis above we treat nonoverlapping extraction regions in each of the sources as independent probes of spectra of SF regions. We have three nonoverlapping subregions in G330.9536, one in G332.8254, and two in Sgr B2(M). The presence of several SF clusters is typical for a H II region. Although different clusters are a part of the same H II region, and thus have similar chemical composition, environmental properties, and they have similar but not equal ages, they nonetheless

can be considered fairly independent probes of EUV spectra of star formation. It is believed that subregions within H II regions are dominated by either one OB star or by a cluster of a few OB stars. In this case, we do not expect that the binary fractions within each nonoverlapping subregion are correlated. Thus, subregions within H II regions can be treated as independent.

In Figure 6 we present the evolution of the production rates of EUV photons with energies above the ionization thresholds of H I, He I, and He II, i.e., $h\nu > 13.6$ eV (Q_0), $h\nu > 24.6$ eV (Q_1), and $h\nu > 54.4$ eV (Q_2), respectively, and the evolution of the slope (γ) of the EUV spectra of $L_\nu \sim \nu^{-\gamma}$, where 13.6 eV $\leq h\nu < 54.4$ eV as a function of metallicity. The variations of spectral parameters are obvious, yet it is still clear that the metallicity alone cannot account for the discrepancy of the model and the observed spectral properties.

6. Conclusion

We observed a sample of four H II regions spanning various stages of H II region evolution with ALMA in the millimeter recombination lines of H I, He I, and He II—H30 α , He30 α , and He⁺48 α , respectively, to derive the shape of the underlying EUV spectra. We find that irrespective of the evolutionary stage of the H II region, the spectra are surprisingly similar to each other and scale with frequency as $L_\nu \sim \nu^{-4.5}$, for 13.6 eV $\leq h\nu < 54.4$ eV (Table 2). We compared this result with model spectra obtained with population-synthesis codes Starburst99 v7.0.1 and BPASS v2.2.1 (Figure 5). Starburst99 and BPASS v2.2.1 single star assumes zero binary fraction, and BPASS v2.2.1 with binary interaction assumes that about 60% of $5M_\odot$ stars are in binaries and with the fraction rising to above 90% for $16 M_\odot$ and higher. We find that the observed spectral slope $\gamma \simeq 4.5 \pm 0.4$ differs from both model predictions. Because we do not know the exact ages of our SF regions, we

compare both models with the data for all ages <30 Myr. If we assume that the ages of the observed SF regions are greater than ~ 7 Myr, then the observationally determined EUV spectral slope lies between the slope obtained with the two population-synthesis codes. This would imply that the binary fraction within our H II regions must be substantially lower than that assumed in BPASS v2.2.1 (see Figure 1 in Stanway & Eldridge 2018).

The technique demonstrated here is a unique probe of EUV spectra, as it is free from uncertainties of extinction corrections and trace ion abundances. The millimeter/submillimeter recombination lines of H I, He I, and He II are reliable probes of the EUV spectra inside SF populations, allowing us to determine the production rate of EUV ionizing photons above ionization thresholds of H I, He I, and He II and reconstruct the properties of the EUV spectra. In this work we applied the technique to Galactic H II regions, but it can be extended to galaxies. Among its most natural and powerful applications is the study of ultraluminous infrared galaxies (see SM13) and star formation in the distant universe, which refers to the period after the end of the Dark Ages ($z \sim 7-15$) and up until the Cosmic Noon ($z \sim 2$). The insight into star formation in the distant universe can be obtained from local analogs for the distant galaxy population (Heckman et al. 2005; Stanway & Davies 2014). The lower metallicity of the gas from which the stars are formed in these galaxies would result in the formation of more massive stars and correspondingly modified EUV spectral properties. There is a longstanding question of exactly which objects—early galaxies or early active nuclei—reionize the universe and whether the observed number counts of these objects are consistent with the reionization requirements (see e.g., Dayal et al. 2020). If the EUV spectrum of low-metallicity SF regions is softer than what was assumed in the previous reionization calculations and models, then it would make it even more difficult for early stars to reionize the universe.

The technique demonstrated here opens a new avenue for studying the EUV spectra, as it allows us to derive reliable observational constraints that can be used to test the predictions of various star formation models in a way that was previously not possible, providing critical insight into photon production rates at $\lambda \leq 912\text{\AA}$. This can help calibrate starburst synthesis models and shed light on properties of star formation in the distant universe and the properties of ionizing radiation during reionization.

We are grateful to Nick Scoville for cowriting the ALMA proposals and collaboration on the initial stages of the paper, to J.J. Eldridge, Susan Clark, David Guszejnov, and to the anonymous referee for their thoughtful comments, which helped improve the manuscript.

L.M.’s stipend at the IAS is provided by the Friends of the Institute for Advanced Study. A part of this work was conducted while L.M. was supported by the SOS NRAO program and as a Groce Fellow at Caltech. L.M. is grateful to Dr. David and Barbara Groce for their kindness and support.

Part of this research was carried out at the Jet Propulsion Laboratory, California Institute of Technology, under a contract with the National Aeronautics and Space Administration.

This paper makes use of the following ALMA data: ADS/JAO.ALMA#2013.1.00111.S and ADS/JAO.ALMA#2016.1.01015. S ALMA is a partnership of ESO (representing its member states),

NSF (USA) and NINS (Japan), together with NRC (Canada) and NSC and ASIAA (Taiwan) and KASI (Republic of Korea), in cooperation with the Republic of Chile. The Joint ALMA Observatory is operated by ESO, AUI/NRAO, and NAOJ.

The National Radio Astronomy Observatory is a facility of the National Science Foundation operated under cooperative agreement by Associated Universities, Inc.

Appendix Ionizing Photon Count, Volume Emission Measures, and EUV Spectra

We use standard notation for the production rates of the ionizing photons above the ionization thresholds of H I, He I, and He II; see Equation (5). We assume that the EUV spectrum in SF regions can be represented by a broken power law as

$$L_\nu = \begin{cases} L_0(\nu/\nu_0)^{-\gamma}, & \nu_0 \leq \nu < \nu_2 \\ L_2(\nu/\nu_2)^{-\gamma_2}, & \nu \geq \nu_2. \end{cases} \quad (\text{A1})$$

Here L_0 , γ , L_2 , and γ_2 are constants, and $L_2 = L_0(\nu_2/\nu_0)^{-\gamma}$ to satisfy continuity at $\nu = \nu_2$. Substituting relations (A1) into Equation (5) we have

$$\begin{aligned} Q_0 &= \frac{L_0/h}{\gamma} \left[1 - \left(\frac{\nu_2}{\nu_0} \right)^{-\gamma} \right] + Q_2, \\ Q_1 &= \frac{L_0/h}{\gamma} \left[\left(\frac{\nu_1}{\nu_0} \right)^{-\gamma} - \left(\frac{\nu_2}{\nu_0} \right)^{-\gamma} \right] + Q_2, \\ Q_2 &= \frac{L_0/h}{\gamma_2} \left(\frac{\nu_2}{\nu_0} \right)^{-\gamma}. \end{aligned} \quad (\text{A2})$$

We can solve this system numerically for C , γ , and γ_2 . The solution can be written analytically if we make use of the fact that $Q_2 \ll Q_0$ and $Q_2 \ll Q_1$. We then get

$$\begin{aligned} \frac{Q_1}{Q_0} &\simeq \frac{\nu_1^{-\gamma} - \nu_2^{-\gamma}}{\nu_0^{-\gamma} - \nu_2^{-\gamma}}, \\ L_0/h &\simeq \frac{\gamma Q_0}{1 - (\nu_2/\nu_0)^{-\gamma}}, \\ \gamma_2 &= \frac{L_0/h - \gamma Q_0}{Q_2} = \gamma \frac{Q_0}{Q_2} \frac{1}{(\nu_2/\nu_0)^\gamma - 1}. \end{aligned} \quad (\text{A3})$$

To derive the ionizing photon production rates Q from the observed EM’s we assume (i) that the gas is in a radiation equilibrium, so that the number of recombinations of each ion species is equal to the number of ionizations producing this ion species per unit time; and (ii) that all ionizing photons are used within the region and none escape. Additionally, in order to obtain analytical solutions, (iii) we are going to disregard the possibility that high-energy photons can be stolen by species with a lower ionizing threshold (for detailed treatment, see, e.g., Osterbrock & Ferland 2006). Thus we have

$$\begin{aligned} Q_0 &\simeq \alpha_B^{\text{H I}} \text{EM}_{\text{H II}}, \quad Q_1 \simeq \alpha_B^{\text{He I}} \text{EM}_{\text{He II}}, \\ Q_2 &\simeq \alpha_B^{\text{He II}} \text{EM}_{\text{He III}}, \end{aligned} \quad (\text{A4})$$

where

$$\begin{aligned}\alpha_B^{\text{H I}} &= 2.59 \times 10^{-13} \text{ cm}^3 \text{ s}^{-1}, \\ \alpha_B^{\text{He I}} &= 2.72 \times 10^{-13} \text{ cm}^3 \text{ s}^{-1}, \\ \alpha_B^{\text{He II}} &= 1.85 \times 10^{-12} \text{ cm}^3 \text{ s}^{-1}\end{aligned}\quad (\text{A5})$$

are recombination coefficients of H I, He I, and He II to all $n \geq 2$ at $T = 10^4$ K.

Combining Equations (A4) and (A3) we get

$$\frac{2.21^\gamma - 1}{4^\gamma - 1} \simeq 0.105 \left(\frac{EM_{\text{He II}}}{10^{60} \text{ cm}^{-3}} \right) \left(\frac{EM_{\text{H II}}}{10^{61} \text{ cm}^{-3}} \right)^{-1}, \quad (\text{A6})$$










$$L_0 \simeq 1.716 \times 10^{22} \frac{\text{erg}}{\text{s Hz}} \left(\frac{EM_{\text{H II}}}{10^{61} \text{ cm}^{-3}} \right) \frac{\gamma}{1 - 0.25^\gamma}, \quad (\text{A7})$$

$$\gamma_2 \simeq 1.4\gamma \times 10^2 \left(\frac{EM_{\text{H II}}}{10^{61} \text{ cm}^{-3}} \right) \left(\frac{EM_{\text{He III}}}{10^{58} \text{ cm}^{-3}} \right)^{-1} [4^\gamma - 1]^{-1}, \quad (\text{A8})$$

$$L_2 = 1.716 \times 10^{22} \frac{\text{erg}}{\text{s Hz}} \left(\frac{EM_{\text{H II}}}{10^{61} \text{ cm}^{-3}} \right) \frac{\gamma}{4^\gamma - 1}. \quad (\text{A9})$$

Using Equation (A6) we can solve for γ , which we then substitute it into the rest of the equations to find L_0 , L_2 , and γ_2 , thus obtaining the intrinsic EUV spectra inside the region.

ORCID iDs

Lena Murchikova  <https://orcid.org/0000-0001-8986-5403>
 Eric J. Murphy  <https://orcid.org/0000-0001-7089-7325>
 Dariusz C. Lis  <https://orcid.org/0000-0002-0500-4700>
 Lee Armus  <https://orcid.org/0000-0003-3498-2973>
 Selma de Mink  <https://orcid.org/0000-0001-9336-2825>
 Kartik Sheth  <https://orcid.org/0000-0002-5496-4118>
 Nadia Zakamska  <https://orcid.org/0000-0001-6100-6869>
 Frank Tramper  <https://orcid.org/0000-0002-5891-0950>
 Martin Elvis  <https://orcid.org/0000-0001-5060-1398>

Lisa Kewley  <https://orcid.org/0000-0001-8152-3943>
 Hugues Sana  <https://orcid.org/0000-0001-6656-4130>

References

- Baldwin, J. A., Phillips, M. M., & Terlevich, R. 1981, *PASP*, **93**, 5
 Crockett, N. R., Bergin, E. A., Neill, J. L., et al. 2014, *ApJ*, **787**, 112
 Crowther, P. A., Caballero-Nieves, S. M., Bostroem, K. A., et al. 2016, *MNRAS*, **458**, 624
 Dayal, P., Volonteri, M., Choudhury, T. R., et al. 2020, *MNRAS*, **495**, 3065
 de Mink, S. E., Pols, O. R., Langer, N., & Izzard, R. G. 2009, *A&A*, **507**, L1
 Eldridge, J. J., Stanway, E. R., Xiao, L., et al. 2017, *PASA*, **34**, e058
 González Delgado, R. M., Leitherer, C., & Heckman, T. M. 1999, *ApJS*, **125**, 489
 Heckman, T. M., Hoopes, C. G., Seibert, M., et al. 2005, *ApJL*, **619**, L35
 Leitherer, C. 2012, in *Astronomical Society of India Conference Series*, Vol. 6, ed. P. Prugniel & H. P. Singh (Pune: Astronomical Society of India), 79
 Leitherer, C., Ekström, S., Meynet, G., et al. 2014, *ApJS*, **212**, 14
 Leitherer, C., Schaerer, D., Goldader, J. D., et al. 1999, *ApJS*, **123**, 3
 Levesque, E. M., Leitherer, C., Ekstrom, S., Meynet, G., & Schaerer, D. 2012, *ApJ*, **751**, 67
 Linden, S. T., Murphy, E. J., Dong, D., et al. 2020, *ApJS*, **248**, 25
 Maeder, A., & Meynet, G. 2000, *A&A*, **361**, 159
 Murphy, E. J., Bremseth, J., Mason, B. S., et al. 2012, *ApJ*, **761**, 97
 Murphy, E. J., Momjian, E., Condon, J. J., et al. 2017, *ApJ*, **839**, 35
 Murphy, T., Cohen, M., Ekers, R. D., et al. 2010, *MNRAS*, **405**, 1560
 Osterbrock, D. E., & Ferland, G. J. 2006, *Astrophysics of Gaseous Nebulae and Active Galactic Nuclei*, 1st edn (Mill Valley, CA: University Science Books)
 Redfield, S. 2006, in *ASP Conf. Ser. 352, The Local Interstellar Medium*, ed. S. J. Kannappan et al. (San Francisco, CA: ASP), 79
 Sana, H., de Mink, S. E., de Koter, A., et al. 2012, *Sci*, **337**, 444
 Scoville, N., & Murchikova, L. 2013, *ApJ*, **779**, 75
 Shull, J. M., Stevans, M., & Danforth, C. W. 2012, *ApJ*, **752**, 162
 Stanway, E. R., & Davies, L. J. M. 2014, *MNRAS*, **439**, 2474
 Stanway, E. R., & Eldridge, J. J. 2018, *MNRAS*, **479**, 75
 Stanway, E. R., Eldridge, J. J., & Becker, G. D. 2016, *MNRAS*, **456**, 485
 Storey, P. J., & Hummer, D. G. 1995a, *yCat*, **6064**, 0
 Storey, P. J., & Hummer, D. G. 1995b, *MNRAS*, **272**, 41
 Towle, J. P., Feldman, P. A., & Watson, J. K. G. 1996, *ApJS*, **107**, 747
 Veilleux, S., & Osterbrock, D. E. 1987, *ApJS*, **63**, 295
 Vink, J. S. 2000, PhD thesis, Universiteit Utrecht
 Werner, K. 2010, *LanB*, **4A**, 109